mater.scichina.com link.springer.com

Published online 7 May 2024 | https://doi.org/10.1007/s40843-023-2817-x
Sci China Mater 2024, 67(7): 2201–2209

Giant in-plane vibrational and transport anisotropy in van der Waals $Ta_2Ni_3Te_5$

Haige Tan[1†], Ying Zhang[1†], Zhisheng Zhao[2†], Changlong Wang[1], Ranran Zhang[3], Shasha Wang[1], Xiang Ma[1], Yan Feng[1], Meng Gu[4], Yalin Lu[1], Juan Jiang[2*], Shunhong Zhang[5*] and Bin Xiang[1*]

ABSTRACT **Recently, layered van der Waals compounds of $Ta_2M_3Te_5$ (M = Ni, Pd) have garnered revived interest due to their appealing potentials to host various exotic electronic states and exhibit nontrivial transport phenomena, such as the Luttinger liquid, quantum spin Hall effect, high-order topology, and superconductivity. In this paper, we report the synthesis of single-crystalline $Ta_2Ni_3Te_5$ and reveal multifold in-plane anisotropic properties rooted in its quasi-one-dimensional bonding feature within each constituent layer. Our technique combines the power of polarized Raman spectroscopy, angle-resolved photoemission spectroscopy, first-principles calculations, and electrical/magneto-transport measurements. The phononic vibrations of chain-like low symmetric layered structure give rise to a highly anisotropic Raman response. The distinct intra- and inter-chain bonding characteristics lead to anisotropic dispersion of both electronic bands and acoustic phonons, which collectively result in giant in-plane mobility anisotropy (2000%) between the [100] and [001] directions, as verified by our electrical transport and Hall effect measurements. Accordingly, the transport behaviors along different in-plane directions also exhibit distinct temperature and magnetic-field dependence. The rich in-plane anisotropy revealed by the present work shows that $Ta_2Ni_3Te_5$ is a promising platform for exploring novel two-dimensional anisotropic electronic dynamics with potential applications in next-generation nanoelectronic devices.**

Keywords: in-plane anisotropy, vibrational and electronic transport anisotropy, quasi-1D layered structure, first-principles calculations, angle-resolved photoemission spectroscopy (ARPES)

INTRODUCTION

Two-dimensional (2D) materials, a focus of materials science, have been rapidly developed in the past two decades marked by the milestone discovery of monolayer graphene [1]. Such materials have received tremendous attention because of their novel electrical, optical, and magnetic properties [2], which are usually distinct from those of their bulk counterparts. Most layered materials discovered at the early stage of the 2D era, such as graphene [2], graphitic silicene [3], h-BN [4,5], transition metal dichalcogenides [6,7], and MXenes [8,9], exhibit in-plane isotropic properties due to their highly symmetric hexagonal lattice. The anisotropy in these materials thus relies on the vertical stacking of constituent layers mediated by van der Waals (vdW) interactions, which contrasts the properties along the in-plane and out-of-plane directions. In contrast, phosphorene, a monolayer form of black phosphorus realized in 2014 [10,11], possesses a puckered honeycomb structure that gives rise to strong in-plane anisotropy with a wealth of fundamental properties [12].

Such remarkable intralayer anisotropy in 2D materials associated with the reduced crystal symmetry not only significantly enriches the in-plane physics for exploitation, but also offers an extra degree of freedom for designing conceptually new directionality-based devices with vast applications [13,14]. After black phosphorene, a plethora of new 2D materials featuring in-plane anisotropy have been discovered and widely studied, ranging from semimetals (e.g., T_d-WTe_2 [15], 1T'-$MoTe_2$ [16], $ZrTe_5$ [17], and $TaIrTe_4$ [18]) to semiconductors (e.g., Ta_2NiS_5 [19], $GeAs_2$ [20], ReS_2 [21], $ReSe_2$ [22], and $PdSe_2$ [23]). However, achieving large anisotropy of conductivity and mobility in air-stable layered materials, which is highly desirable for designing conceptually new nanoelectronic devices, remains challenging. Recently, layered GaTe is reported as a new 2D material with gate-tunable electrical conductivity anisotropy [24], but the material's air sensitivity and lack of oxidation resistance hinder its potential applications in nanoelectronics.

Questing for new in-plane anisotropic materials, we pay attention to $Ta_2Ni_3Te_5$, a representative member in the family of layered vdW compounds $A_2M_{1,3}X_5$ (A = Ta, Nb; M = Pd, Ni; X = Se, Te). Studies of this class of ternary materials date back to the 1990s [25], and recently, revived interest has been evoked in the community by their versatile potential as platforms for achieving exotic transport properties such as the Luttinger liquid state,

[1] Department of Materials Science & Engineering, CAS Key Lab of Materials for Energy Conversion, Anhui Laboratory of Advanced Photon Science and Technology, University of Science and Technology of China, Hefei 230026, China
[2] Department of Physics and School of Emerging Technology, University of Science and Technology of China, Hefei 230026, China
[3] Anhui Key Laboratory of Condensed Matter Physics at Extreme Conditions, High Magnetic Field Laboratory, Chinese Academy of Sciences, Hefei 230031, China
[4] Department of Materials Science and Engineering, Southern University of Science and Technology, Shenzhen 518055, China
[5] International Center for Quantum Design of Functional Materials (ICQD), University of Science and Technology of China, Hefei 230026, China
[†] These authors contributed equally to this work.
[*] Corresponding authors (emails: jjiangcindy@ustc.edu.cn (Jiang J); szhang2@ustc.edu.cn (Zhang S); binxiang@ustc.edu.cn (Xiang B))

quantum spin Hall effect [26], quadrupole topological insulator state [27], and pressure-induced superconductivity [28]. From a crystallographic perspective, $Ta_2Ni_3Te_5$ consists of rhombus-like Ta_2Ni_2 clusters that act as building blocks within each layer. These clusters are first linked into 1D chains and then loosely joined to form a 2D layer, exhibiting a quasi-1D feature. Despite the long history of research and a potential renaissance akin to the case of phosphorene [29], the fundamental structural, electronic, and transport properties of this compound, which are likely in-plane anisotropic given the distinctive crystal structure, have not yet been experimentally exploited.

In this paper, we report the discovery of multifold giant in-plane anisotropy in $Ta_2Ni_3Te_5$ arising from its quasi-1D layered structure with low in-plane crystal symmetry. The single-crystal sample is prepared using a two-step chemical vapor transport approach, and the two natural growth edges of the sample are unequivocally identified to be the in-plane crystallographic axes, along which the layered compound exhibits distinct bonding characteristics. The resultant anisotropic atomic vibrations are revealed by polarized Raman spectroscopy and further elucidated by first-principles density functional perturbation theory calculations. High-precision angle-resolved photoemission spectroscopy (ARPES) measurements and first-principles calculations consistently reveal that the valence bands exhibit distinct dispersion along the [001] and [100] directions, which lead to differences of hole effective mass by one order of magnitude. Based on the deformation potential theory, we further unravel that the hole mobility also possesses pronounced in-plane anisotropy. The spatially resolved electrical transport measurements directly confirm such predictions, quantifying the anisotropy ratio between the [100] and [001] directions to be as high as 600% for the low-temperature longitudinal conductivity, and even more pronounced (2000%) for the hole mobility, in good agreement with calculations. The magneto-transport properties are also found to be directional when an out-of-plane magnetic field is applied, which may be implemented to harness the anisotropy.

Our work identifies and characterizes a novel and prototypical layered material with giant in-plane phononic and electrical anisotropy, offering new opportunities for exploring the directional transport of heat or charge within the 2D layer. These results may spark further interest in investigating the anisotropy's interplay with the intrinsic topologically nontrivial boundary (edge or corner) states or various external physical (strain, electrical, magnetic, or optical) fields.

EXPERIMENTAL SECTION

Growth and characterization of the $Ta_2Ni_3Te_5$ single crystal

Single crystals of $Ta_2Ni_3Te_5$ were prepared *via* a two-step process. In the first step, we prepared polycrystalline powder samples of $Ta_2Ni_3Te_5$ *via* high-temperature solid-state reactions. The mixture of constituent elements Ta, Ni, and Te with a molar ratio of 2:3:5 was transferred to a silica tube and sealed under vacuum. Then, the sealed tube was heated to 900°C for 48 h in a Muffle furnace. In the second step, involving vaporing and recrystallization, an appropriate amount of iodine was added to the resultant powder to promote the transport of vapors. The powder was then sealed into a new silica tube under vacuum and heated in a two-zone tube furnace with a temperature gradient of 950–850°C for seven days. Afterwards, the single crystals of $Ta_2Ni_3Te_5$ were obtained at the cold end of the tube.

The crystal structure was characterized by using powder X-ray diffraction (XRD, Ultima IV) with a Cu Kα radiation source. The thickness of the exfoliated samples on SiO_2/Si was characterized by using atomic force microscopy (AFM, Dimension Icon). The chemical compositions were characterized by using scanning electron microscopy (SEM, GeminiSEM 500) and energy-dispersive X-ray spectroscopy (EDS, Oxford Aztec). The chemical stoichiometry and valence states were characterized by using X-ray photoelectron spectroscopy (XPS, Kratos AXIS SUPRA+). The interplanar spacing of the samples was characterized by using high-resolution scanning transmission electron microscopy (HRSTEM, JEM-ARM200F).

Angle-dependent Raman scattering measurements

Raman spectra were recorded in the backscattering geometry with a 532-nm laser as an excitation source (HORIBA J.Y. T64000). Low temperature was maintained by a closed-cycle He-cryostat (ST500) attached to the spectrometer.

ARPES measurements

ARPES measurements were performed at beamline 21-ID-1 of the National Synchrotron Light Source II (NSLS II) equipped with a Scienta DA30 electron analyzer. The photon energy used for the experiment was 56 eV, which covered the Z-Γ-X plane with an overall energy resolution better than 15 meV. The samples were cleaved *in situ* to achieve a fresh surface for the measurement in a vacuum chamber at a pressure below 2×10^{-11} Torr (1 Torr = 133.322 Pa). All measurements were performed at 15 K.

Fabrication of Hall devices for transport measurements

We fabricated six annular Hall electrodes with a width of 7 μm and a central diameter of 20 μm by Ultraviolet Lithography on a silicon substrate with 285-nm-thick SiO_2. The 8-nm-thick Ti and 25-nm-thick Au as the conducting media were plated onto a Hall electrode by magnetron sputtering. The device was fabricated by a dry-transfer technique. The synthesized $Ta_2Ni_3Te_5$ sample was mechanically exfoliated into thin films with tape and then transferred onto the PDMS. Then, we transferred the sample to a Hall electrode through an accurate microscopic transfer platform (Metatest, E1-T), with its short edge aligned parallel to one pair of electrodes.

All the electronic transport measurements were performed in a physical property measurement system (PPMS) fabricated by Quantum Design, in which the basic temperature and magnetic field of the platform could reach 1.8 K and 9 T, respectively. The testing current was 100 μA, and the magnetic field was applied perpendicular to the sample.

First-principles calculations

First-principles calculations based on density functional theory (DFT) were performed to investigate the electronic properties of the $Ta_2Ni_3Te_5$ compound, as implemented in the Vienna *Ab initio* Simulation Package (VASP) [30]. The projector-augmented wave method [31] and a plane-wave basis with a cutoff of 550 eV were adopted to treat the core and valence electrons, respectively. The Perdew-Burke-Ernzerhof (PBE) functional within the Generalized Gradient Approximation (GGA) [32] was used to describe the electron exchange and correlation. The crystal structure of $Ta_2Ni_3Te_5$ was taken from the Materials

Project database [33] and relaxed by DFT calculations, with the energy and atomic force convergence thresholds set to 10^{-6} eV and 10^{-3} eV Å^{-1}, respectively. The Brillouin zone was sampled by an 8 × 2 × 2 Monkhorst-Pack *k*-mesh. Spin-orbit interaction was self-consistently included in the calculations.

RESULTS AND DISCUSSION

Growth and the characterization of the crystal

$Ta_2Ni_3Te_5$ crystallizes into a layered structure with the space group of *Pnma* (No. 62). The orthogonal primitive cell contains two layers stacked along the crystallographic *b* axis and bonded with weak vdW interactions, which are related by inversion symmetry [26], as illustrated in Fig. 1a–c. In each constituent layer, the Ta and Ni atoms are sandwiched between two layers of Te atoms. Each Ta atom bonds with five Te atoms, forming a $TaTe_5$ polyhedron, while the Ni atoms occupy their tetrahedral vacancies. The $TaTe_5$ motifs are interconnected in edge- and corner-shared modes along the [100] and [001] directions, respectively, giving rise to the quasi-1D bonding characteristics illustrated in Fig. 1c. To characterize the structure and crystallinity of the as-grown $Ta_2Ni_3Te_5$ sample, we carryout X-ray powder diffraction (XRD), selected area electron diffraction (SAED), HRSTEM, XPS (Note S1 and Fig. S1), and scanning electron microscopy (SEM) analyses. The XRD spectrum and HRSTEM patterns appear in Fig. 1d, e, respectively, consistently revealing that the $Ta_2Ni_3Te_5$ sample possesses high crystallinity. The SAED pattern, shown in the inset of Fig. 1e, coincides well with the simulated pattern from the reported crystal structure. Importantly, the low-magnification TEM image (Fig. S2) suggests that the direction of the short side of the rectangular-shaped $Ta_2Ni_3Te_5$ flake is perpendicular to the (002) crystal plane. Accordingly, the orientation of the long and short sides of the $Ta_2Ni_3Te_5$ flake can be unambiguously assigned to the [100] and [001] crystallographic axes of the single crystal, respectively, which facilitates our further exploration of the angle-dependent vibrational and transport properties to identify compelling intralayer anisotropies. AFM is utilized to characterize the morphology of the $Ta_2Ni_3Te_5$ flake; the yield topography (displayed in Fig. 1f) exhibits a smooth and clean surface, and the AFM height profile (inset of Fig. 1f) characterizes the flake thickness to be ~6.5 nm. The stoichiometry characterized by energy dispersive X-ray spectroscopy spectra (Fig. S3) reveals some Te-deficient features of the material. However, by comparing the optical image and Raman spectra measured on the same sample immediately and eight months after it was exfoliated and transferred onto the silicon substrate, we found that the degradation under sufficient air exposure was rather slow (Fig. S4), indicating that the $Ta_2Ni_3Te_5$ sample was air-insensitive.

Angle-dependent Raman scattering

To explore the atomic vibrational properties of this $Ta_2Ni_3Te_5$ with a unique quasi-1D layered crystal structure, we conduct angle-dependent Raman scattering measurements. A thin film exfoliated from the synthesized $Ta_2Ni_3Te_5$ sample is transferred onto a silicon substrate with 285-nm-thick SiO_2 (Fig. S5a) for Raman spectroscopic studies. The incident lasers are linearly polarized along the X and Y directions for two individual measurements, corresponding to the two directions of the

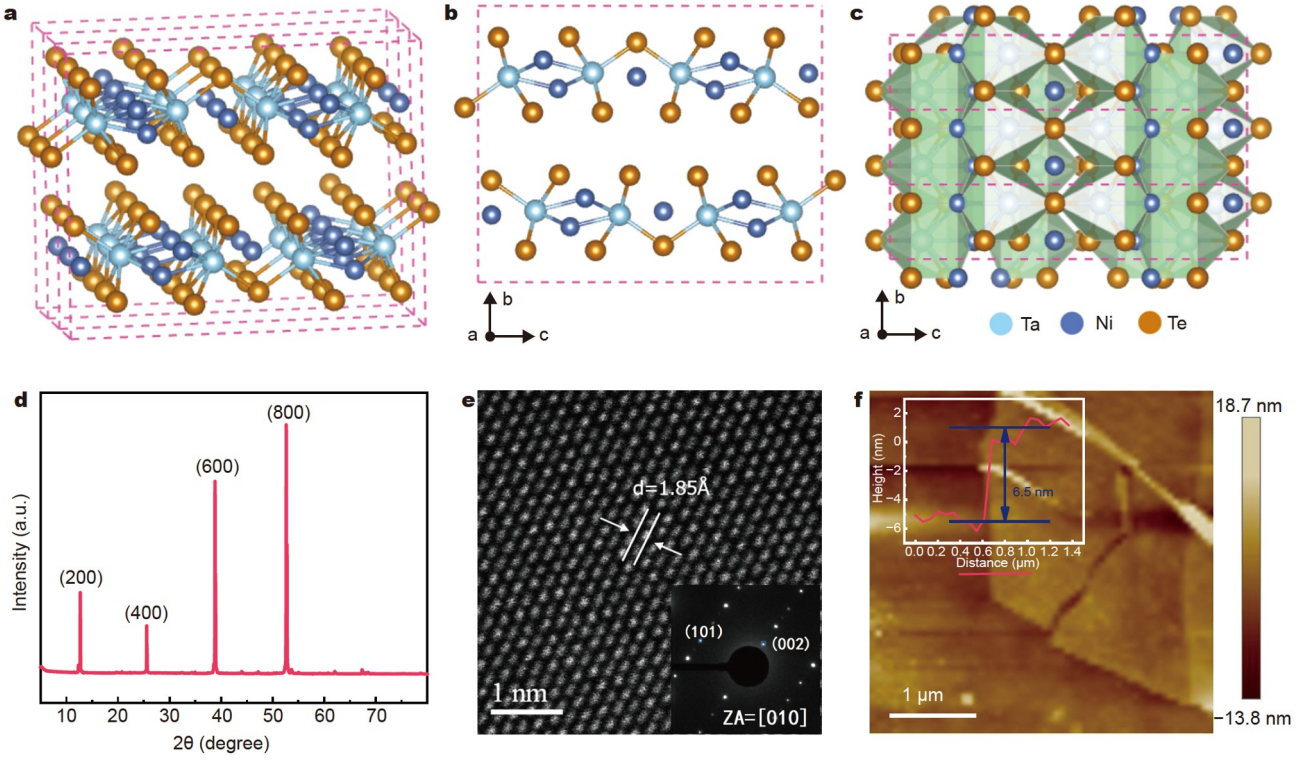

Figure 1 Structural characterizations of the synthesized $Ta_2Ni_3Te_5$. (a–c) Crystal structures: (a) perspective view; (b) view from [100] direction, showing the layered geometry; (c) view from [010] direction, showing the quasi-1D feature within each layer. (d) X-ray diffraction pattern. (e) HRSTEM image of a representative sample. Inset: SAED pattern along the [010] axis. (f) AFM image of a thin flake mechanically exfoliated from the synthesized sample. Inset: Height profile corresponding to the dashed line cut near the sample edge.

naturally growing crystallographic edges. Fig. 2a shows the polarized Raman spectra measured at 4.25 K, demonstrating that the Raman intensities at different peak positions are strongly angle-dependent. The Raman spectra also exhibit evident variation upon increasing temperatures (Fig. S5). It is thus necessary to explore where the Raman anisotropy stems from and whether it can be manipulated by temperature. To gain atomic insights, we calculate the phonon frequencies and vibration patterns of the normal modes at the Brillouin zone center and identify Raman-active modes *via* group-theoretical symmetry analyses. To elucidate the microscopic mechanism of the Raman anisotropy, we select three characteristic modes for detailed analyses, with the peaks located at 115.3, 175.1, and 167.5 cm^{-1}, as marked by the dark green vertical dashed lines in Fig. 2a. The temperature dependence of Raman intensity for these three modes along the X and Z directions are displayed in Fig. 2b. The former two exhibit opposite preferred polarizations throughout a wide temperature range, while the third mode has a more complex dependence. By comparing with the calculation results, these three characteristic peaks are assigned to the normal modes with irreducible representations of B_{3u}, B_{3g}, and B_{1u}, respectively, whose atomic vibrations are sketched in Fig. 2c–e. The B_{3u} mode at 115.3 cm^{-1} is the main peak with the vibration direction of most atoms parallel to the [001] direction, thus harboring a more pronounced Raman intensity when the polarization of the incident laser is along the Z direction. In contrast, the B_{3g} mode located at 175.1 cm^{-1} mediates phonon vibrations mainly along the [100] direction, giving rise to enhanced Raman response when the laser is polarized along the X direction. For the B_{1u} mode containing mixed vibration components along both [001] and [001] directions, the Raman intensities polarized along X and Z are comparable at low

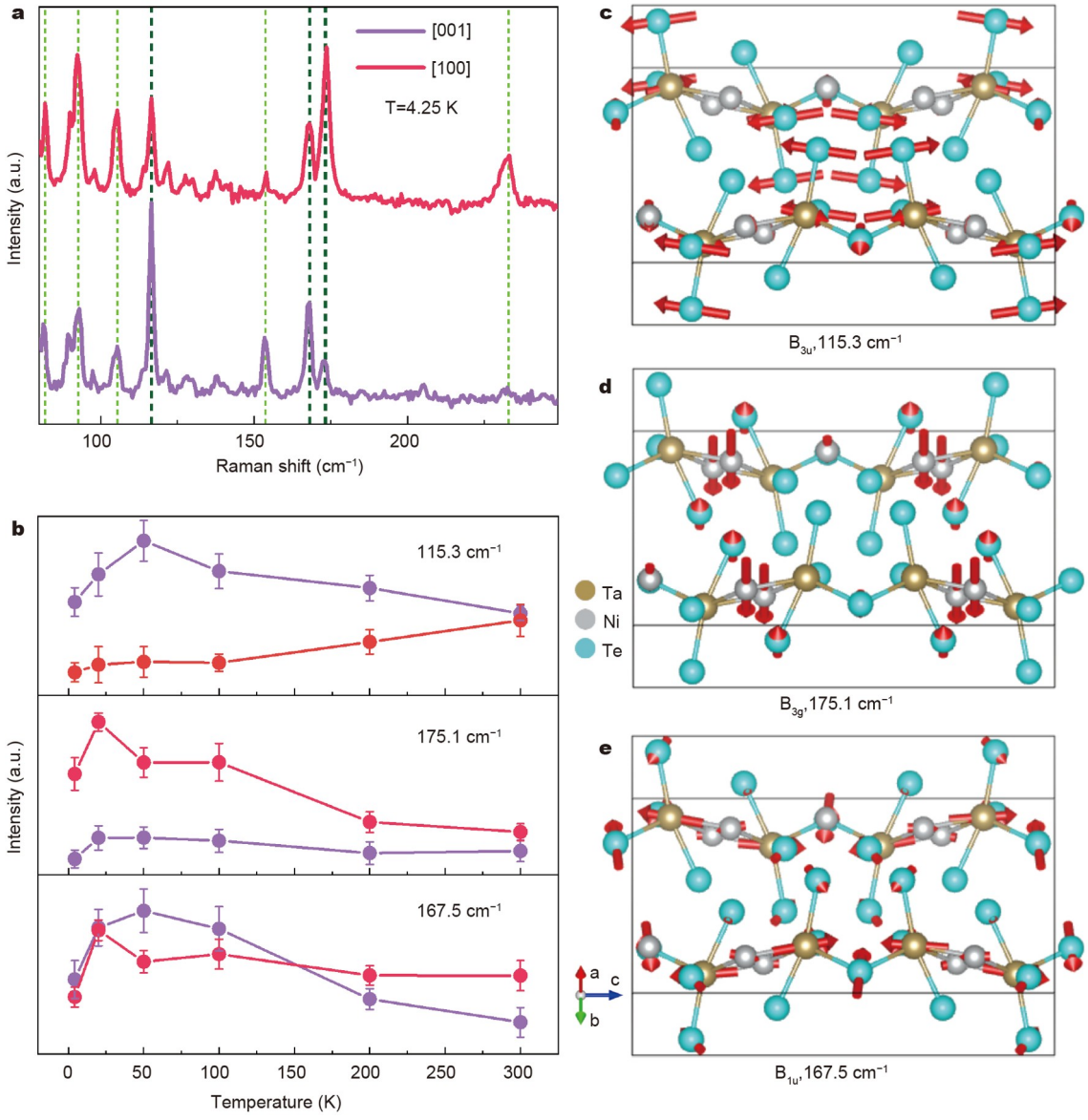

Figure 2 Angle-dependent Raman scattering spectra of $Ta_2Ni_3Te_5$. (a) Raman spectra with laser polarized along the [001] and [100] directions, respectively, both measured at 4.25 K. (b) Temperature dependence of Raman intensity for selected modes (marked by dark green dashed lines in (a)) with the Raman shifts (from top to bottom) of 115.3, 175.1, and 167.5 cm^{-1}, respectively. (c–e) Calculated phonon vibrational patterns for three Raman-active modes in (b), with the arrows denoting the atomic displacement directions of the normal mode.

temperatures, but they differentiate as the temperature rises. Other Raman-active modes present vibrational anisotropy as well (Fig. S6). Through these temperature-dependent measurements, we confirm that no obvious changes appear in the Raman-scattering peak positions (Fig. S5), indicating that no significant shifts exist in the vibrational modes, and the structure does not undergo structure phase transition. More importantly, as the temperature increases, a decreasing trend is observed in the disparity of peak intensities when the laser is polarized along the [001] and [100] directions, respectively, especially for the main Raman shifts at 115.3 and 175.1 cm^{-1}; they approach convergence at room temperature (Fig. 2b). These modes with a polarized vibration pattern (Fig. 2c, d) contribute greatly to the Raman anisotropy of the system, and they exhibit a thermal evolution resembling the electronic transport. In contrast, the vibration of the B1u mode with frequency 167.5 cm^{-1} is non-unidirectional (Fig. 2e), so its Raman polarization temperature dependence exhibits more complicated behavior. These mode- and polarization-dependent Raman responses signify that the atomic vibrations in $Ta_2Ni_3Te_5$ also exhibit significant anisotropy. In fact, our calculated phonon spectrum (Fig. S7) suggests that the phonon dispersion and group velocity along the X and Z directions also present strong anisotropy, implying that heat transport mediated by lattice vibrations may also be directional within the layer, which remains to be proven in the future. In the rest of the present work, we focus on the electronic structure and charge dynamics, and electron-phonon scattering by the anisotropic acoustic phonon modes is also investigated.

Electronic band structures with strong anisotropy

To investigate the electronic properties of layered $Ta_2Ni_3Te_5$, we perform ARPES measurements and first-principles calculations based on density functional theory (DFT), both capable of providing details of the dispersion of electronic bands in the momentum space. Here, we focus on the in-plane dispersions, in particular, dispersions along the Γ-X and Γ-Z directions, which correspond to the [100] and [001] crystallographic axes, respectively. The low-energy electronic structure measured by ARPES is presented in Fig. 3a, b, revealing a strong anisotropy of band dispersion, especially the valence bands near the Fermi level, which dominates hole transport properties. The DFT-calculated band structure (Fig. 3c) consistently reproduces the anisotropic characteristic, and it further identifies the material as a semiconductor with a mini-gap of tens of meV. The band edges are located in the vicinity of the Brillouin zone center, in accordance with previous studies [27,28]. In Fig. 3d, we further map the band energies within the k_x-k_z momentum plane, from which one can clearly observe the Fermi contour anisotropy of the hole bands. The evolution along k_y is less dispersive, implying much weaker interlayer bonding in accordance with the vdW nature of the material.

Anisotropic electronic transport properties

Recalling that the vdW layers in $Ta_2Ni_3Te_5$ are stacked along the [010] direction, we can expect that the compound hosts strongly in-plane anisotropic transport properties. We pay specific attention to the hole bands that hold more pronounced anisotropy between the [100] and [001] directions. To gain further insights into the hole carrier dynamics, we calculate their mobility by using the deformation potential theory proposed by Bardeen and Shockley [34]. This simplified method treats the electron-phonon interaction by considering the long-range acoustic phonon as the primary scattering source; this technique has proven to provide valuable insights regarding the transport of band-edge charge carriers. The analytical expression for temperature-dependent carrier mobility $\mu(T)$ of 3D semiconducting materials can be written as

$$\mu_{3D}(T)=\frac{2(2\pi)^{1/2}e\hbar^4C}{3(k_BT)^{3/2}|m^*|^{5/2}E_1^2}, \quad (1)$$

with C, m^*, and E_1 being the elastic constant, carrier effective mass, and deformation potential of the material along specific crystallographic direction, respectively. Values for C and E_1 can be obtained *via* parabolic and linear fitting of the strain energy and valence band maximum energy shift under small magnitude uniaxial strains, respectively, while m^* can be estimated by parabolic fitting of the band dispersion near the valence band maximum with respect to momenta (Fig. S8). Here, e, $\hbar$, and k_B are, respectively, the elementary charge, reduced Planck constant, and Boltzmann constant. From the results summarized in Table 1, we can see that C, m_h^*, and E_1 all exhibit pronounced differences between the [100] and [001] directions, among which m_h^* has the strongest anisotropy, with the value along [001] nearly one order of magnitude larger than that along [100]. This aligns with the observed anisotropic dispersion (Fig. 3a–c) and energy contours of the hole-bands (Fig. 3d, e) in the electronic structure obtained by ARPES and DFT. As a collective consequence of the anisotropy of these quantities, the hole mobility along the two directions differs by nearly one order. This giant mobility difference implies that the in-plane electrical transport behavior is highly anisotropic.

To study the predicted anisotropic transport properties, we fabricate an electrical-transport device from the $Ta_2Ni_3Te_5$ flakes (see the Experimental Section for details). An optical image of the device is shown in the insert of Fig. 4a, with each two adjacent electrodes separated by an angle of 60°. The thickness of the device is approximately 114 nm (Fig. S9). As mentioned above, the orientation of the long side of the flake sample is along [100], while the short side is along [001]. We use the four-terminal method to measure the electrical resistivity (ρ) as a function of temperature (T) with the current applied along both [100] and [001] directions, respectively. Fig. 4a shows that the electrical resistivity is on the order of 10^{-2} Ω·cm, and it decreases with the increase of temperatures, revealing the semiconducting behavior of $Ta_2Ni_3Te_5$ accords with our first-principles electronic structure characterization as well as previous studies [35]. More importantly, the resistivity along the [001] direction is much larger than that along the [100] direction, especially at low temperatures. To further exploit the transport anisotropy, we measure the in-plane resistivity of $Ta_2Ni_3Te_5$ along six different directions in contact with the electrodes at different temperatures. The results are plotted in Fig. 4b in polar coordinates, with 0° and 180° representing the resistivity measured with the current applied along the [001] direction. The resistivities of the other two pairs of electrodes (60° and 120°) exhibit symmetry and are very close to each other regardless of the measuring temperatures. In contrast, the resistivity along [001] has a strong temperature dependence and is much higher than those along other directions at low temperatures. At 3 K, the pronounced in-plane transport anisotropy, as characterized by the ratio of maximum over minimum resistivities, can reach ~600%.

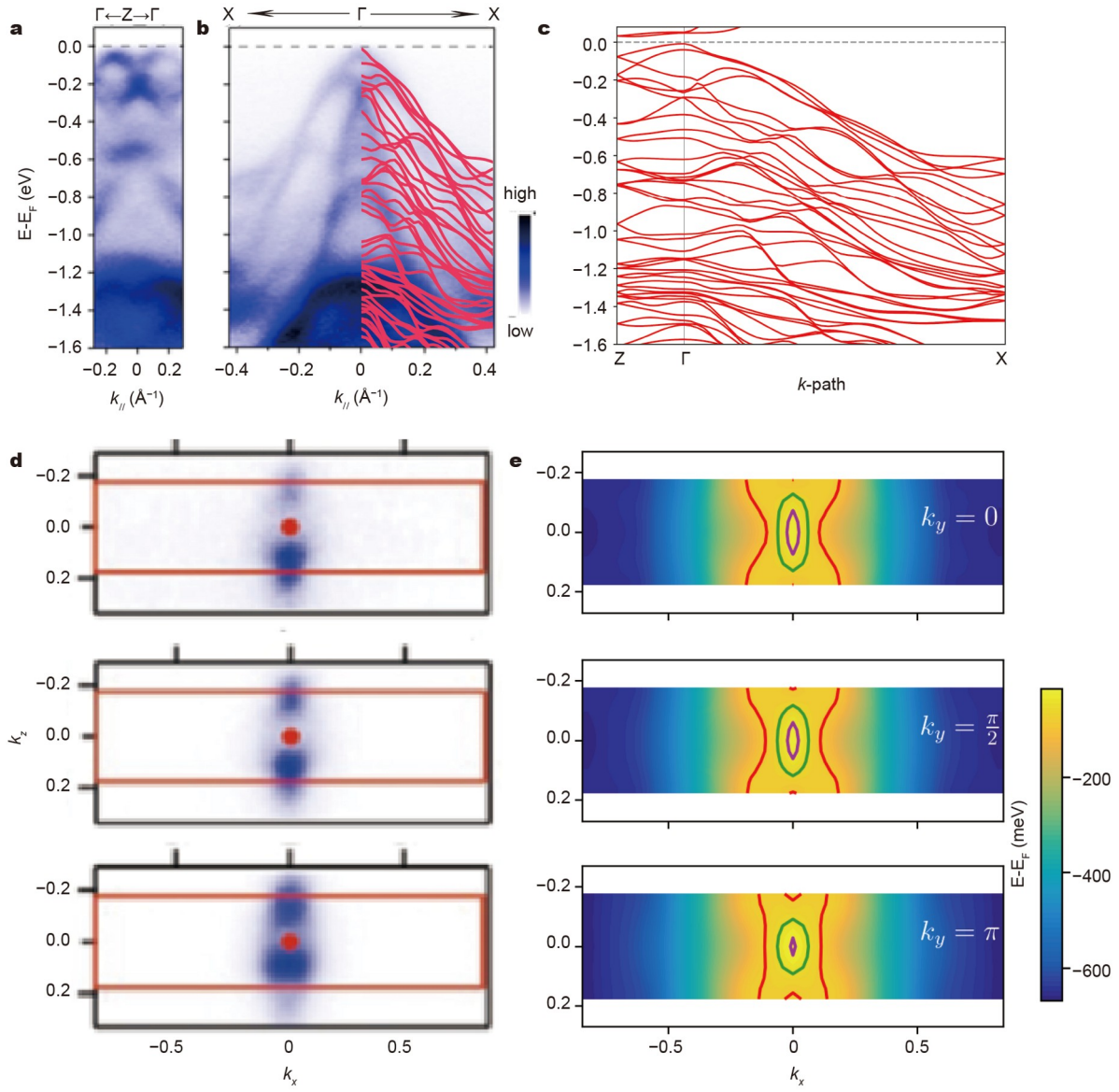

Figure 3 Electronic band structures of $Ta_2Ni_3Te_5$ obtained from (a, b) ARPES and (c) first-principles calculations. In (b), the first-principles bands are also super-positioned to show consistency. (d) ARPES constant-energy contours of $Ta_2Ni_3Te_5$ at −20, −50, and −80 meV, respectively. (e) DFT bands in the form of k_x-k_z slice cuts, with k_y = 0, 1/4, and 1/2, respectively. The valence band energies relative to the Fermi level are mapped in color, and the energy contours corresponding to −20, −50, and −80 meV are respectively plotted in purple, green, and red.

Table 1 In-plane ([100] and [001]) hole effective masses (m_0 is the rest mass of electrons), elastic constants, deformation potentials, and hole mobilities of $Ta_2Ni_3Te_5$ calculated from the first-principles band structure and based on the deformation potential theory. The right column presents the ratio of each spatial dependent quantity to demonstrate the anisotropy.

	$\overline{X}$-Γ-X [100]	$\overline{Z}$-Γ-Z [001]	Ratio
m_h^* (m_0)	−0.15	−1.02	0.15
C (GPa)	44.3	63.7	0.70
E_1 (eV)	−15.1	−8.35	1.81
μ_h at 300 K (cm^2 V^{-1} s^{-1})	1418	53	26.75

The revealed in-plane anisotropic lattice vibration and charge transport of $Ta_2Ni_3Te_5$ tied to the chain-like crystal structure imply that the response of some fundamental properties to external fields could also exhibit transparent spatial dependence. Inspired by these insights, we perform magneto-transport measurements at 3 K along the [001] and [100] directions, respectively, by applying an out-of-plane magnetic field perpendicular to the *ac* plane and along the *b* axis as illustrated by the inset of Fig. 4a. One can observe from Fig. 4c that the longitudinal resistivity (ρ_{xx}) shows a clear direction dependence

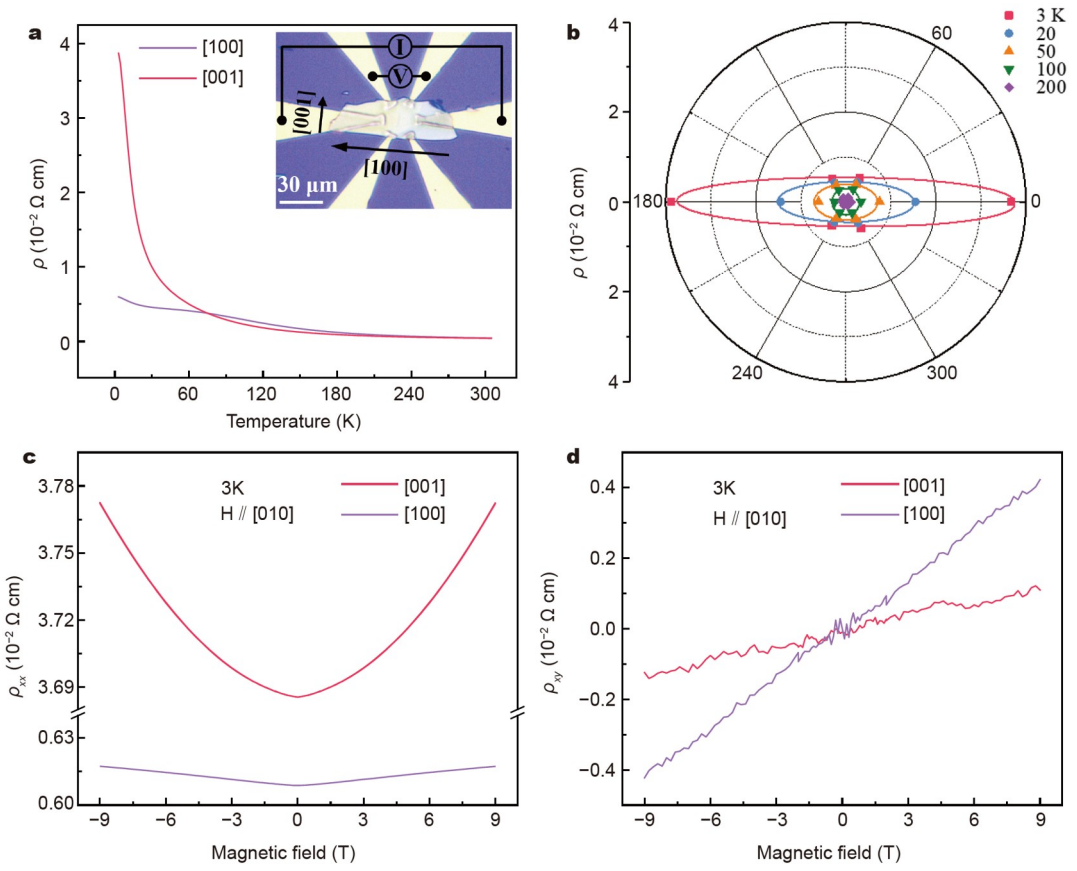

Figure 4 Angle-resolved electronic transport properties of $Ta_2Ni_3Te_5$. (a) Temperature dependence of the resistivity for electric current applied in [001] and [100], with the inset showing an optical image of the device for measurements. (b) Angle-dependent resistivity at different temperatures. Spatially anisotropic (c) longitudinal (ρ_{xx}) and (d) Hall (ρ_{xz}) resistivities at 3 K, as functions of the magnetic field applied along the *b*-axis.

and exhibits unsaturated behavior in both measured directions even when the applied magnetic field reaches its upper limit of 9 T. The maximum magnetoresistance (*MR*) values along the [100] and [001] directions at $\mu_0 H$ = 9 T are respectively 2.36% and 1.40%, calculated using the equation:

$$MR = \frac{\rho_{xx}(H_{\max}) - \rho_{xx}(H_0)}{\rho_{xx}(H_0)} \times 100\%, \quad (2)$$

where $\rho_{xx}(H_{\max})$ and $\rho_{xx}(H_0)$ are the longitudinal resistivity under the maximum ($\mu_0 H_{\max}$ = 9 T) and zero magnetic field, respectively. Fig. 4d shows a linear dependence of the Hall resistivity (ρ_{xz}) on the applied magnetic field ($\mu_0 H$), and the slopes of ρ_{xz}-$\mu_0 H$ curves along both [100] and [001] directions are positive, suggesting that the major charge carriers in $Ta_2Ni_3Te_5$ are holes. The directional carrier mobility μ can be calculated by using

$$\mu = \sigma_{xx} \frac{d\rho_{xz}}{dB}, \quad (3)$$

where the derivative dρxz/d*B* is the Hall coefficient ($B = \mu_0 H$), whose magnitude along the [001] and [100] directions are determined to be 3.53 × 10^{-9} and 1.61 ×10^{-8} Ωm T^{-1}, respectively. The longitudinal conductivity σ_{xx} can be calculated from the resistivity as follows:

$$\sigma_{xx} = \frac{\rho_{xx}(H_0)}{[\rho_{xx}(H_0)]^2 + [\rho_{xy}(H_0)]^2}, \quad (4)$$

with the values along the [001] and [100] directions being respectively 2710.03 and 16,426.02 Ω^{-1} m^{-1}. Accordingly, the corresponding hole mobilities are 0.096 and 1.93 cm^2 V^{-1} s^{-1}, respectively. The ratio of the difference reaches 2000%, quantitively consistent with predictions from deformation potential theory; this attests to the conclusion that the hole mobility possesses giant anisotropy between the directions of [001] and [100]. We note that the hole mobilities calculated from deformation potential theory are much higher than those extracted from Hall measurements, which can be understood because the simplified model only accounts for the scattering of long-wave acoustic phonons and neglects other scattering sources in the actual material, such as optical phonons, electron-electron scatterings, and impurities/defects. We also note that the ratios of mobilities along the two in-plane crystal axes from calculations and experiments are in nice agreement, confirming the anisotropic nature. Given that the $Ta_2Ni_3Te_5$ compound has been demonstrated to harbor nontrivial band topology, it would be interesting to study the interplay between the anisotropic bulk charge transport and the boundary propagation of carriers protected by topology, which is a topic for future work.

CONCLUSIONS

In summary, we synthesized the vdW material $Ta_2Ni_3Te_5$ featuring chain-like quasi-1D constituent layers and identified strong multifold intralayer anisotropy associated with the material's unique geometry and bonding characteristics. Raman spectroscopy indicated that the atomic vibrations were anisotropic, with distinct responses to laser polarized along different

in-plane crystallographic directions. Combining ARPES and first-principles calculations, we identified the anisotropic feature of energy dispersion in momentum space, based on which we deduced that the hole effective mass and carrier mobility should exhibit pronounced in-plane anisotropy. Our angle-dependent electrical transport measurements not only confirm this speculation but also reveal highly anisotropic hole-dominated conductivity that can be more significant at lower temperatures. This anisotropic conductivity and mobility overall outperform most similar materials (see Table S1 for comparison with previously reported layered materials with in-plane transport anisotropy). Such anisotropy has been demonstrated to be an essential property for developing high-gain digital inverters, polarization-sensitive photodetectors, and many other electronic or optoelectronic devices. Moreover, a higher anisotropic ratio is always more desirable for these applications. Its air-insensitivity endows $Ta_2Ni_3Te_5$ with extra merit for device integration and application. The multifold anisotropy highlights the important role of intralayer quasi-1D bonding in the performance of the layered $Ta_2Ni_3Te_5$ compound. This material can stimulate extensive interest in exploring rich physics under reduced dimensionality and crystal symmetry, and this research is potentially even more intriguing in the presence of topologically nontrivial boundary states. Such research results offer new opportunities for developing conceptually new 2D electronic devices.

Received 13 November 2023; accepted 8 February 2024; published online 7 May 2024

1 Novoselov KS, Geim AK, Morozov SV, *et al.* Electric field effect in atomically thin carbon films. Science, 2004, 306: 666–669
2 Wang M, Huang M, Luo D, *et al.* Single-crystal, large-area, fold-free monolayer graphene. Nature, 2021, 596: 519–524
3 Vogt P, De Padova P, Quaresima C, *et al.* Silicene: Compelling experimental evidence for graphenelike two-dimensional silicon. Phys Rev Lett, 2012, 108: 155501
4 Lee JS, Choi SH, Yun SJ, *et al.* Wafer-scale single-crystal hexagonal boron nitride film *via* self-collimated grain formation. Science, 2018, 362: 817–821
5 Wang L, Xu X, Zhang L, *et al.* Epitaxial growth of a 100-square-centimetre single-crystal hexagonal boron nitride monolayer on copper. Nature, 2019, 570: 91–95
6 Allain A, Kang J, Banerjee K, *et al.* Electrical contacts to two-dimensional semiconductors. Nat Mater, 2015, 14: 1195–1205
7 Radisavljevic B, Radenovic A, Brivio J, *et al.* Single-layer MoS_2 transistors. Nat Nanotech, 2011, 6: 147–150
8 Wyatt BC, Rosenkranz A, Anasori B. 2D MXenes: Tunable mechanical and tribological properties. Adv Mater, 2021, 33: 2007973
9 Naguib M, Kurtoglu M, Presser V, *et al.* Two-Dimensional nanocrystals produced by exfoliation of Ti_3AlC_2. Adv Mater, 2011, 23: 4248–4253
10 Li L, Yu Y, Ye GJ, *et al.* Black phosphorus field-effect transistors. Nat Nanotech, 2014, 9: 372–377
11 Liu H, Neal AT, Zhu Z, *et al.* Phosphorene: An unexplored 2D semiconductor with a high hole mobility. ACS Nano, 2014, 8: 4033–4041
12 Liu X, Chen K, Li X, *et al.* Electron matters: Recent advances in passivation and applications of black phosphorus. Adv Mater, 2021, 33: 2005924
13 Gong C, Zhang Y, Chen W, *et al.* Electronic and optoelectronic applications based on 2D novel anisotropic transition metal dichalcogenides. Adv Sci, 2017, 4: 1700231
14 Li L, Han W, Pi L, *et al.* Emerging in-plane anisotropic two-dimensional materials. InfoMat, 2019, 1: 54–73
15 Choi YB, Xie Y, Chen CZ, *et al.* Evidence of higher-order topology in multilayer WTe_2 from Josephson coupling through anisotropic hinge states. Nat Mater, 2020, 19: 974–979
16 Zhu M, Zhao Y, Feng Q, *et al.* Linear dichroism and nondestructive crystalline identification of anisotropic semimetal few-layer $MoTe_2$. Small, 2019, 15: 1903159
17 Seo SB, Nah S, Sajjad M, *et al.* Completely anisotropic ultrafast optical switching and direction-dependent photocarrier diffusion in layered $ZrTe_5$. Adv Opt Mater, 2023, 11: 2201544
18 Liu Y, Gu Q, Peng Y, *et al.* Raman signatures of broken inversion symmetry and in-plane anisotropy in Type-II Weyl semimetal candidate $TaIrTe_4$. Adv Mater, 2018, 30: 1706402
19 Li L, Gong P, Wang W, *et al.* Strong in-plane anisotropies of optical and electrical response in layered dimetal chalcogenide. ACS Nano, 2017, 11: 10264–10272
20 Li L, Gong P, Sheng D, *et al.* Highly in-plane anisotropic 2D $GeAs_2$ for polarization-sensitive photodetection. Adv Mater, 2018, 30: 1804541
21 Wang YY, Zhou JD, Jiang J, *et al.* In-plane optical anisotropy in ReS_2 flakes determined by angle-resolved polarized optical contrast spectroscopy. Nanoscale, 2019, 11: 20199–20205
22 Hong M, Zhou X, Gao N, *et al.* Identifying the non-identical outermost selenium atoms and invariable band gaps across the grain boundary of anisotropic rhenium diselenide. ACS Nano, 2018, 12: 10095–10103
23 Zhu R, Gao Z, Liang Q, *et al.* Observation of anisotropic magnetoresistance in layered nonmagnetic semiconducting $PdSe_2$. ACS Appl Mater Interfaces, 2021, 13: 37527–37534
24 Wang H, Chen ML, Zhu M, *et al.* Gate tunable giant anisotropic resistance in ultra-thin GaTe. Nat Commun, 2019, 10: 2302
25 Tremel W. Isolated and condensed Ta_2Ni_2 clusters in the layered tellurides $Ta_2Ni_2Te_4$ and $Ta_2Ni_3Te_5$. Angew Chem Int Ed Engl, 1991, 30: 840–843
26 Guo Z, Yan D, Sheng H, *et al.* Quantum spin Hall effect in $Ta_2M_3Te_5$ (M = Pd, Ni). Phys Rev B, 2021, 103: 115145
27 Guo Z, Deng J, Xie Y, *et al.* Quadrupole topological insulators in $Ta_2M_3Te_5$ (M = Ni, Pd) monolayers. npj Quantum Mater, 2022, 7: 87
28 Yang H, Zhou Y, Wang S, *et al.* Pressure-induced nontrivial Z_2 band topology and superconductivity in the transition metal chalcogenide $Ta_2Ni_3Te_5$. Phys Rev B, 2023, 107: L020503
29 Ling X, Wang H, Huang S, *et al.* The renaissance of black phosphorus. Proc Natl Acad Sci USA, 2015, 112: 4523–4530
30 Kresse G, Furthmüller J. Efficient iterative schemes for *ab initio* total-energy calculations using a plane-wave basis set. Phys Rev B, 1996, 54: 11169–11186
31 Blöchl PE. Projector augmented-wave method. Phys Rev B, 1994, 50: 17953–17979
32 Elmér R, Berg M, Carlén L, *et al.* K^+ emission in symmetric heavy ion reactions at subthreshold energies. Phys Rev Lett, 1996, 77: 4884–4886
33 Jain A, Ong SP, Hautier G, *et al.* Commentary: The materials project: A materials genome approach to accelerating materials innovation. APL Mater, 2013, 1: 011002
34 Bardeen J, Shockley W. Deformation potentials and mobilities in non-polar crystals. Phys Rev, 1950, 80: 72–80
35 Zheng X, Lee H, Weisgraber TH, *et al.* Ultralight, ultrastiff mechanical metamaterials. Science, 2014, 344: 1373–1377

Acknowledgements This work was supported by the Innovation Program for Quantum Science and Technology (2021ZD0302800), the National Natural Science Foundation of China (11904350, 12174362), Anhui Provincial Natural Science Foundation (2008085QA30), Shenzhen Science and Technology Program (KQTD20190929173815000), Guangdong Innovative and Entrepreneurial Research Team Program (2019ZT08C044), and the National Synchrotron Radiation Laboratory (KY2060000177). This research was partially conducted at the Center for Micro and Nanoscale Research and Fabrication, USTC.

Author contributions Tan H designed the experiments and prepared the samples. Tan H, Zhang Y, Zhao Z, Wang C, Zhang R, Wang S, Ma X, and Feng Y performed the measurements and characterizations for most of the analysises. Zhang S conducted the first-principles calculations and provided theoretical support. All authors contributed to the discussion of the results.

Tan H, Zhang Y, Zhao ZS, Jiang J, Zhang S, and Xiang B participated in writing and revising the manuscript.

Conflict of interest The authors declare that they have no conflict of interest.

Supplementary information Experimental details and supporting data are available in the online version of the paper.

Haige Tan is a doctoral student at the Department of Materials Science & Engineering, University of Science and Technology of China. His main research interests include the synthesis and characterization of 2D materials, and the fabrication of nanodevices.

Ying Zhang received her PhD degree from the Department of Materials Science & Engineering, University of Science and Technology of China in 2023. Then, she joined the School of Electronic Engineering, Huainan Normal University as a lecturer. Her research interests mainly focus on the fabrication of 2D vdW magnetic materials and their applications in spintronic devices.

Zhisheng Zhao is a doctoral student at the Department of Physics, University of Science and Technology of China. His main research interest is investigating the novel electronic states with ARPES and MBE.

Juan Jiang joined the School of Emerging Technology, University of Science and Technology of China as a professor since 2020. Her research interests mainly focus on the electronic structure of quantum materials, including unconventional superconductors, topological materials, and 2D materials.

Shunhong Zhang received his PhD degree in 2016 from Peking University. He joined the University of Science and Technology of China in 2018. His research interests include low-dimensional magnetic materials, topological materials, and light-element-based nanomaterials.

Bin Xiang received his PhD degree in physics from Peking University in July 2005. During his postdoc appointment at the University of California at San Diego (2005–2007), his research focuses on the nanomaterials and nanodevice applications. During his postdoc appointments at the University of California at Berkeley and Lawrence Berkeley National Lab (2007–2012), his research has expanded into the area of *in-situ* probing of nanoscale functional materials in TEM. In 2012, Prof. Xiang started his faculty appointment at the Department of Materials Science and Engineering, University of Science and Technology of China, focusing on 2D functional Materials including hetero-integration of 2D quantum materials and exploration of their spintronics applications.

范德华材料$Ta_2Ni_3Te_5$中巨大的面内振动和输运各向异性

谈海歌[1†], 张颖[1†], 赵志生[2†], 王昌龙[1], 张冉冉[3], 王莎莎[1], 马响[1], 冯艳[1], 谷猛[4], 陆亚林[1], 姜娟[2*], 张顺洪[5*], 向斌[1*]

摘要 目前, $Ta_2M_3Te_5$ (M = Ni, Pd)层状范德华化合物可承载各种奇异电子态, 且具有表现出非平凡输运现象的诱人潜力, 因而重新引起人们的兴趣. 其特征有Luttinger液体、量子自旋霍尔效应、高阶拓扑结构和超导电性. 本文中, 我们报道了单晶$Ta_2Ni_3Te_5$的合成, 并揭示了其在每个具有准一维键合特征的层内的多重平面内各向异性. 我们的技术结合了偏振拉曼光谱、角度分辨光电发射光谱、第一性原理计算和电/磁输运测量的能力. 链状低对称层状结构的声子振动产生了高度各向异性的拉曼响应, 不同的链内和链间键合特性导致电子带和声学声子的各向异性色散, 这共同导致[100]和[001]方向之间的巨大平面内迁移率各向异性(2000%). 这一结果与我们的电输运和霍尔效应测量结果相符. 因此, 沿不同平面内方向的输运行为也表现出不同的温度和磁场依赖性. 本工作揭示的丰富的面内各向异性表明, $Ta_2Ni_3Te_5$是探索新型二维各向异性电子动力学的一个很有前途的平台, 在下一代纳米电子器件中具有潜在的应用前景.